Eleventh International Conference on Computational Fluid Dynamics (ICCFD11), Maui, HI, USA, July 11-15, 2022

ICCFD11-2022-2703

Dynamic QSV-LES of hypersonic boundary layer transition delay via porous walls over a blunt cone

V. C. B. Sousa*, V. Wartemann***, A. Wagner*** and C. Scalo*,**
Corresponding author: vsousa@purdue.edu

* School of Mechanical Engineering, Purdue University, USA
** School of Aeronautics and Astronautics, Purdue University, USA
*** German Aerospace Center (DLR), Göttingen, Germany

Abstract: Numerical simulations of hypersonic boundary layer transition delay on a 7°-half-angle cone with a 2.5 mm-nose tip radii via an impedance boundary condition that numerically replicates the effects of a porous carbon fibre reinforced carbon matrix ceramics (C/C) surface. The flow conditions studies are related to experiments performed at the High Enthalpy Shock Tunnel Göttingen (HEG) at the Reynolds numbers $Re_m = 4.06 \cdot 10^6$ and $6.40 \cdot 10^6$ m^{-1} with a freestream Mach number of $M_\infty = 7.4$. The stability of the base flow is analyzed over impermeable and porous walls via both pulse-perturbed axisymmetric simulations and through solving linearized governing equations. Simulated results for second-mode spatial growth rates match linear predictions showing the dynamic large-eddy simulation (LES) quasi-spectral procedure's capability of numerically preserving the instability wave dynamics. Three-dimensional transitional LES were then performed with the introduction of grid independent pseudorandom pressure perturbations. Numerical predictions were compared against experimental measurements regarding the frequency content of the disturbances in the transitional region with fairly good agreement capturing the shift to lower frequencies. Such shift is caused by the formation of near-wall low-temperature streaks that concentrate the pressure disturbances at locations with locally thicker boundary layers forming trapped wavetrains that can persist into the turbulent region. Additionally, results indicate that the presence of a porous surface representative of a C/C material does not affect turbulence significantly and simply shifts its onset downstream.

Keywords: Hypersonic Flow, Turbulence Transition, Compressible Boundary Layer, Large-Eddy Simulations.

1 Introduction

Laminar-to-turbulent transition has critical implications on the design, performance and safe operation of hypersonic vehicles. At such high speeds, aerodynamic and thermal loads, which are already significant under laminar flow conditions, can increase dramatically in the presence of turbulence. Reed et al. (1997) studied a low-Earth orbit hypersonic flight vehicle in fully laminar and fully turbulent flow conditions and concluded that the requirements for the thermal protection systems (TPS) double in the latter case due to a factor of five increase in wall-heat flux caused by laminar-to-turbulent transition. Considering a low disturbance environment such as the flight conditions, transition to turbulence over smooth surfaces in hypersonic conditions is governed by the dynamics of the second modal instability. Mack's studies on the evolution of these and higher modes (Mack, 1990) in two dimensional boundary layers stressed the importance of second-mode attenuation in any attempt to increase the transitional Reynolds number in high speed flows.

Previous studies showed, through theoretical and experimental studies, the capability of ultrasonically absorbing coatings (UACs) to mitigate the second mode. Malmuth et al. (1998) proved through Linear Stability Theory (LST) the capability of ultrasonically absorbing coatings (UACs) to mitigate the second-

Color/Symbol	Re_m $[1/m]$	M_∞ $[-]$	p_∞ $[Pa]$	T_∞ $[K]$	ρ_∞ $[kg/m^3]$
★	$1.46 \cdot 10^6$	7.3	789	267	0.0102
●	$4.06 \cdot 10^6$	7.4	2129	268	0.0276
◆	$6.40 \cdot 10^6$	7.4	3083	248	0.0432

Table 1: Nominal flow parameters from Wagner et al. (2013). Throughout the manuscript, each of these flow conditions will be represented by the color here assigned.

mode. Experiments performed at Mach 5 at the T-5 hypersonic wind tunnel located at Caltech (Fedorov et al., 2001; Rasheed et al., 2002) provided the first validation of this principle by using a cone with a half angle of 5 degrees with two different surfaces: one smooth and impermeable, and the other perforated with regularly spaced micro holes. They reported that the porous surface was capable of doubling the transitional Reynolds number in comparison with the smooth surface. Inspired by these results and the need for any realizable technology for boundary layer control to be symbiotic with thermal protection systems (TPS), Wagner et al. (2013) established the use of carbon-carbon (C/C) UACs in controlling second-mode waves through experiments at Mach 7.5 in the DLR High Enthalpy Shock Tunnel Göttingen (HEG).

Previously, the effects of porous walls in the flow were accounted for only for one frequency component at a time (Egorov et al., 2008; Wang and Zhong, 2010, 2011; Lukashevich et al., 2012). The current work models the porous walls effects on the whole frequency spectrum of the boundary layer transition and also in the fully turbulent regime. This is achieved by building upon work by Scalo et al. (2015), who introduced a technique of implementing a time domain impedance boundary condition (TDIBC) capable of imposing broadband acoustic effects of a porous surface, and efforts by Sousa et al. (2019), who showed C/C's attenuation effect on a broadband second mode disturbance advecting over an axisymmetric conical boundary layer. More recently, a similar framework was used by Chen and Scalo (2021) to study the porosity effects on turbulent channel flows at supersonic and hypersonic bulk Mach numbers (M_b) and it was revealed that sufficiently high porosity can trigger the presence streamwise-travelling waves in the near-wall region.

Ultimately, the goal of the current work is to capture the effects of second-mode propagation in a three-dimensional spatially developing boundary layer over assigned broadband wall-impedance representative of a C/C-based surface. The goal is to investigate the influence of microscale distributed wall porosity on the full transition path to turbulence by replicating the experiments performed by (Wagner et al., 2013).

2 Problem Statement

2.1 Computational Setup

The numerical study performed in this work is based on experiments conducted by Wagner et al. (2013) in the DLR High Enthalpy Shock Tunnel Göttingen (HEG). A complete description of such facility can be found in Hannemann et al. (2018). Axisymmetric (section 3) and three-dimensional (section 4) large-eddy simulations (LES) are carried out for the hypersonic boundary layer flow on a 2.5 mm blunt tip cone for $Re_m = 4.06 \cdot 10^6$ m^{-1} and $6.40 \cdot 10^6$ m^{-1}. A list of all experimental flow conditions is reported in table 1.

The axisymmetric setup is used to validate the current numerical implementation against linear stability predictions made for the second-mode growth rate. This step is important to test the second-mode attenuation caused by the broadband time domain impedance boundary condition (TDIBC) as well as to demonstrate the dynamic capability of the QSV-LES closure (section 2.2), which minimally affects the second-mode wave dynamics. The three-dimensional simulations are then used to study the flow's characteristics in transitional and fully turbulent flow conditions, inspired by Wagner et al. (2013)'s experiments.

The initial condition for the blunt nose simulations was acquired from an external precursor calculation performed by the DLR FLOWer code − a three-dimensional parallel hybrid multi-grid code, validated for hypersonic flows (Kroll and Fassbender, 2006). In section 3, the matching between the steady Navier-Stokes calculations performed in this study and the precursor calculation for the blunt cone is addressed. To avoid the computational costs associated with the very thin boundary layer near the leading edge of the cone, the inlet of the computational domain in this study is located at $x_i = 0.045$ m downstream from the sharp cone tip, while the outlet is located at $x = L_x$ m (see table 2) further downstream, as shown in figure 1. The streamwise extent of the computational domain L_x is chosen based on previous experimental results as the

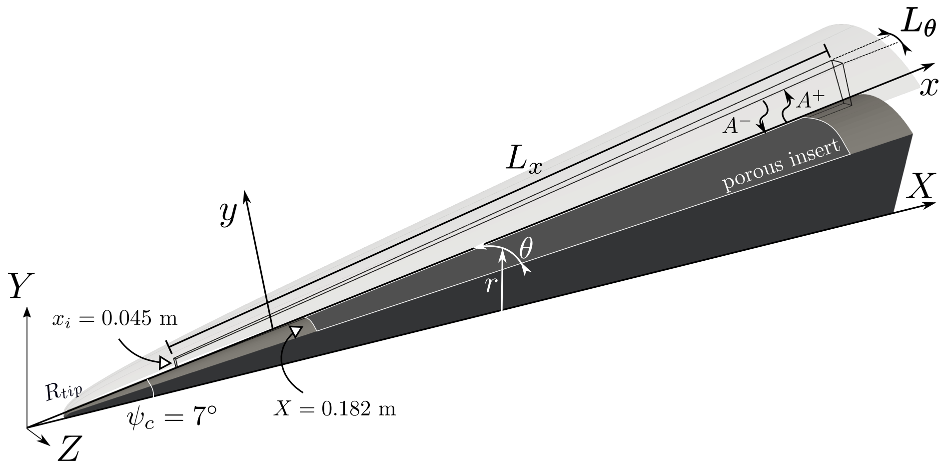

Figure 1: Hypersonic boundary layer transition delay simulations computational setup over a 7° half angle cone with $R_{tip} = 0$ and 2.5 mm. The A^- and A^+ indicate the incident and reflected waves from a surface, related to the implementation of the time domain impedance boundary condition (TDIBC) described in section 2.3. When active, the impedance boundary, used to replicate porosity effects, starts at $X = 0.182$ m matching Wagner et al. (2013)'s experiments.

L_x		Re_m	
		$4.06 \cdot 10^6$ m^{-1}	$6.40 \cdot 10^6$ m^{-1}
R_{tip}	2.5 mm	0.9 m	0.8 m

Table 2: Streamwise extent (L_x) of the computational domain (figure 1) for the different flow conditions and cone geometries considered. Actual nose tip radius for sharp experimental results is 0.1 mm.

smallest distance needed to be able to capture the full transition path to turbulence for both impermeable and porous surface cases.

At the inlet and top boundaries, a Dirichlet boundary condition is used to input the flow velocity calculated by the analytical procedure or by a precursor simulation. Outlet conditions are homogeneous Neumann for all flow quantities. At the wall, Dirichlet conditions are used to impose no-slip, no penetration and, when active, the time domain impedance boundary conditions (TDIBC) used to model the porous surface. This approach allows to model the acoustic response of a C/C-composed surface without the need to resolve its intricate geometrical structure and is a way to retain high resolution on the flow side by removing the grid resolution requirements that would be needed to capture the acoustic wave propagation in the pores. Due to the short duration of the test run, the surface of the model does not have time to heat up and thus can be assumed to be isothermal with a temperature of 300 K.

Sponge layers are used at all non-solid boundaries. The inflow and outflow sponges extend into the domain by $0.03L_x$, while the top boundary sponge is 5% of the local domain height. The inlet sponge is used to weakly impose inflow boundary conditions, while the outlet sponge prevents the formation of upstream traveling disturbances propagating in the subsonic portion of the boundary, while suppressing flow fluctuations convecting downstream before they interact with the outflow computational boundary.

2.2 Filtered Governing Equations In Curvilinear coordinates

High-order structured compact-finite-difference simulations are carried out with the objective of capturing the perturbation evolution with minimum numerical dissipation and high resolving power for a given amount of points per wavelength. Additionally, a dynamic sub-filter scale (SFS) model via the Quasi-Spectral Viscosity (QSV) closure (Sousa and Scalo, 2022), capable of performing both shock capturing and turbulence modeling, is leveraged to promote numerical stability upon three-dimensional turbulent breakdown while remarkably preserving the second-mode wave dynamics (see figures 5). This results in the ability of the model to achieve grid convergence of the transition location (figure 7), which is important for this study focused on transition delay.

The filtered compressible Navier-Stokes equations in generalized curvilinear coordinates are presented hereafter following previous work by Jordan (1999) and Nagarajan et al. (2007), who developed the incompressible and compressible LES methodologies in such context respectively. Assume the existence of a known, invertible mapping between $\mathbf{y}$, the physical cartesian reference frame and $\mathbf{x}$, the contravariant curvilinear coordinate system,

$$x^i = x^i(y^1, y^2, y^3), \tag{1}$$
$$y^i = y^i(x^1, x^2, x^3), \tag{2}$$

where x^i and y^i are the i-th coordinate of each respective system of reference. Following, consider the curvilinear equivalent of Favre filtering,

$$\check{f} = \frac{\overline{J\rho f}}{\overline{J\rho}} \tag{3}$$

where J is the Jacobian of the transformation, the determinant of the Jacobi matrix ($J_{ij} = \partial y^i / \partial x^j$). Then, the filtered governing equations are defined as,

$$\frac{\partial \overline{J\rho}}{\partial t} + \frac{\partial}{\partial x^j}(\overline{J\rho}\check{v}^j) = 0, \tag{4}$$

$$\frac{\partial \overline{J\rho}\check{v}^i}{\partial t} + \frac{\partial}{\partial x^j}(\overline{J\rho}\check{v}^i\check{v}^j + \overline{Jp}g^{ij} - J\check{\sigma}^{ij} + \overline{J\rho}\tau^{ij}) = -\Gamma^i_{qj}(\overline{J\rho}\check{v}^q\check{v}^j + \overline{Jp}g^{qj} - J\check{\sigma}^{qj} + \overline{J\rho}\tau^{qj}), \tag{5}$$

$$\frac{\partial \overline{JE}}{\partial t} + \frac{\partial}{\partial x^j}(\overline{J(E+p)}\check{v}^j + J\check{Q}^j) = \frac{\partial}{\partial x^k}(J\check{\sigma}^{ij}g_{ik}\check{v}^k) - \frac{\partial \overline{J\rho}C_p q^j}{\partial x_j}, \tag{6}$$

and the relevant SFS terms are,

$$\tau^{ij} = \widecheck{v^i v^j} - \check{v}^i\check{v}^j, \quad \text{and} \quad q^j = \widecheck{T v^j} - \check{T}\check{v}^j. \tag{7}$$

Subfilter contributions resulting from the nonlinearities involving the dependency of molecular viscosity or conductivity on temperature have been neglected following Vreman et al. (1995), who showed those are negligible compared to other SFS terms. Following Nagarajan et al. (2003), the SFS kinetic energy advection, $\mu_j = \widecheck{v^k v^k v^j} - \check{v}^k\check{v}^k\check{v}^j$, and the SFS turbulent heat dissipation, $\epsilon = \partial(\overline{\sigma^{ij} v^i})/\partial x^j - \partial\check{(}\sigma^{ij}\check{v}^i)/\partial x^j$, terms are also neglected.

The tensors responsible for mapping a curvilinear physical space into a Cartesian reference space are the covariant and contravariant metric tensors, respectively,

$$g_{ij} = \frac{\partial y^i \partial y^j}{\partial x^k \partial x^k} \quad \text{and} \quad g^{ij} = \frac{\partial x^k \partial x^k}{\partial y^i \partial y^j}, \tag{8}$$

as well as the Christoffel symbol of the second kind,

$$\Gamma^i_{qj} = \frac{\partial x^i}{\partial y^l}\frac{\partial^2 y^l}{\partial x^q \partial x^j}. \tag{9}$$

In the derivation of these equations, the metric tensors and Christoffel symbols are assumed to be varying slowly over the spatial support of the filter kernel, therefore leading to additional negligible sub-filter flux terms.

In the curvilinear frame of reference the total energy, the viscous stress tensor and the heat flux vector are described by slightly modified relations described below:

$$\frac{\overline{Jp}}{\gamma - 1} = \overline{JE} - \frac{1}{2}\overline{J\rho}g_{ij}\check{v}^i\check{v}^j - \frac{1}{2}\overline{J\rho}g_{ij}\tau^{ij}, \tag{10}$$

$$\check{\sigma}^{ij} = \mu\left(g^{jk}\frac{\partial \check{v}^i}{\partial x^k} + g^{ik}\frac{\partial \check{v}^j}{\partial x^k} - \frac{2}{3}g^{ij}\frac{\partial \check{v}^k}{\partial x^k}\right), \tag{11}$$

$$\check{Q}^j = -kg^{ij}\frac{\partial \check{T}}{\partial x^i}. \tag{12}$$

Ultimately, the QSV closures for τ^{mn} and q^n when applied to generalized curvilinear coordinates are

$$\tau^{mn} = -C_{\tau^{mn}}\sum_{k=1}^{3}\frac{1}{2}\left(g^{nk}\mathcal{D}^{mk}\frac{\partial \ddot{v}^m}{\partial x^k} + g^{mk}\mathcal{D}^{nk}\frac{\partial \ddot{v}^n}{\partial x^k}\right), \tag{13}$$

$$q^n = -C_q\sum_{k=1}^{3}g^{nk}\mathcal{D}^{kk}\frac{\partial \ddot{T}}{\partial x^k}. \tag{14}$$

where there is no summation implied in the m and n indices. The above relation is a clarification on the notation used in Sousa and Scalo (2022). Here, the double dot superscript indicates the filter-modulated quantities, defined in curvilinear coordinates as

$$\frac{\partial \ddot{v}^m}{\partial x^k} = \frac{\partial \check{v}^m}{\partial x^k} * \left(1 - \widetilde{G}_{\mathrm{qsv}}\right), \tag{15}$$

$$\frac{\partial \ddot{T}}{\partial x^k} = \frac{\partial \check{T}}{\partial x^k} * \left(1 - \widetilde{G}_{\mathrm{qsv}}\right), \tag{16}$$

where $*$ is the convolution operator and,

$$\hat{\widetilde{G}}_{\mathrm{qsv}} = w\left[1 - \beta\hat{\widetilde{G}}_{\mathrm{Pade}}\left(\alpha\right) + (1-\beta)\hat{\widetilde{G}}_{\mathrm{Fejer}}\right], \tag{17}$$

is the QSV's filter modulation transfer function, comprised by a weighted average between a Padé and a Fejér filter. Additionally, $\mathcal{D}^{mn} = \upsilon^m(\check{v}^n)\ell^n$ is the dissipation magnitude tensor, comprised by a length scale related to the computational grid spacing, $\ell^n = \overline{\Delta}^n$, and the sub-filter velocity scale

$$\upsilon^m(\check{v}^n) = \sqrt{\frac{2E^m_{k_c}\left(\check{v}^n\right)}{\overline{\Delta}^m}}. \tag{18}$$

Again, there is no summation implied in the m and n indices. The full description of the spectral modulation operation, done via $\widetilde{G}_{\mathrm{qsv}}$, and of the estimation of the energy content near the grid cutoff, performed via $E^m_{k_c}\left(\check{v}^n\right)$, can be found in Sousa and Scalo (2022). Lastly, the default values of the coefficients $C_{\tau^{mn}}$, C_q, w, α and β were used in the current work.

The filtered compressible Navier-Stokes equations are discretized in space using a sixth-order accurate compact finite difference method with a staggered grid arrangement (Lele, 1992) and in time using a third order accurate explicit Runge-Kutta method. The numerical strategy used yields spectral-like resolution properties, being able to solve the perturbation evolution inside the boundary layer with minimum numerical dissipation and with high accuracy for a given amount of points per wavelength (Nagarajan et al., 2003). Additionally, the QSV closure has a dynamic property, being only active near areas where nonlinear effects are relevant and preserving the structure of ultrasonic transitional waves.

The generic curvilinear coordinate system transformation applied in the scope of this work maps the physical domain cartesian coordinates ($y^1 = X, y^2 = Y, y^3 = Z$) into (and from) the cylindrical coordinate system ($x^1 = X, x^2 = r, x^3 = \theta$), where the equations are ultimately solved (see figure 1). Additionally, the boundary layer coordinates x and y are also used being a natural way of displaying results of the flow over a conical geometry.

2.3 Time-Domain Impedance Boundary Conditions (TDIBC)

In this work, the acoustic effect of the porous walls is modeled via the imposition of a normal complex impedance, $Z_n(\omega)$, at the boundary defined as the ratio of complex pressure oscillations and the velocity component normal to the boundary in the frequency domain

$$Z_n(\omega) = \frac{1}{\rho_0 a_0} \frac{\hat{p}(\omega)}{\hat{u}_n(\omega)} \tag{19}$$

where $\rho_0 a_0$ is the base impedance, used as a normalization parameter. Impedance in the tangential directions can also be defined, relating instantaneous shear with slip velocity at the interface.

Another important assumption behind (19) is the linearity of the acoustics inside the pores and, for the problem being studied this is an expected behavior for two reasons. First, the thermoviscous dissipation imposed on the waves traveling inside the pores is sufficiently high to ensure rapid attenuation wave amplitude. Second, the low density and pressure environment considered inhibits wave steepening (Thirani et al., 2020), making acoustic nonlinearities in the pores unlikely to be important.

Reflections off an impedance boundary can be exactly imposed by the knowledge of its normal impedance when the assumption of a locally acting surface is valid (Kinsler et al., 1999). Such hypothesis is valid in the current case because the C/C material in question is highly anisotropic (not shown), with the pore structure primarily aligned in the wall-normal direction and small orifice sizes compared to the boundary layer thickness. Moreover, Fedorov et al. (2003) performed a parametric study allowing various degrees of wall-slip velocities, demonstrating that the inviscid nature of the second-mode instability waves makes tangential impedance effects not as relevant as they would be in otherwise viscous dominated instabilities. Therefore, the acoustic effects of a porous C/C surface in the flow can be modeled using only the normal impedance as a boundary condition.

Imposing directly the normal impedance at the boundary is impractical since its magnitude approaches infinity as frequency goes to zero. To overcome this, different formulations using either the reflection coefficient ($\hat{R}$) or the wall softness ($\hat{S}$), defined as

$$\hat{R} = \frac{1 - Z_n(\omega)}{1 + Z_n(\omega)}; \quad \hat{S}(\omega) = \hat{R}(\omega) + 1, \tag{20}$$

were developed, for these quantities are bounded in amplitude when a passive boundary is considered.

To apply a complex impedance in a numerical simulation, one needs to transform it to the time domain. The time domain impedance boundary condition (TDIBC) is implemented in the current numerical scheme as a function of the wall softness ($\hat{S}$) based on the formalism of Fung and Ju (2004) and the numerical integration of the methodology in a compressible Navier-Stokes solver by Scalo et al. (2015) and subsequent work by Lin et al. (2016) and Douasbin et al. (2018). In the current numerical scheme, we fit the complex wall softness $\hat{S}(\omega)$ with a set of complex poles and residues,

$$\hat{S}(\omega) = \frac{2}{1 + Z_n(\omega)} \approx \sum_{k=1}^{n_o} \left[\frac{\mu_k}{s - p_k} + \frac{\mu_k^*}{s - p_k^*} \right], \tag{21}$$

in such a way that their frequency domain response is constrained so that it satisfies the causality, passivity and reality constraints (Rienstra, 2006). In equation (21), n_o is the number of oscillators, μ_k the residues, p_k the poles, and $s = j\omega$. The fitted frequency response is transformed to time domain via an inverse Laplace transform,

$$S(t) \approx \sum_{k=1}^{n_o} \left[\mu_k e^{p_k t} + \mu_k^* e^{p_k^* t} \right], \tag{22}$$

and imposed as inviscid fluxes at the boundary. In equation (22), the superscript (*) denotes complex conjugate.

The fit in the frequency domain is performed following the vector fitting procedure described by Gustavsen and Semlyen (1999), where least square approximation is performed iteratively to relocate the poles and residues and accurately represent the complex response of the function to be fitted in a given interval. Figure 2

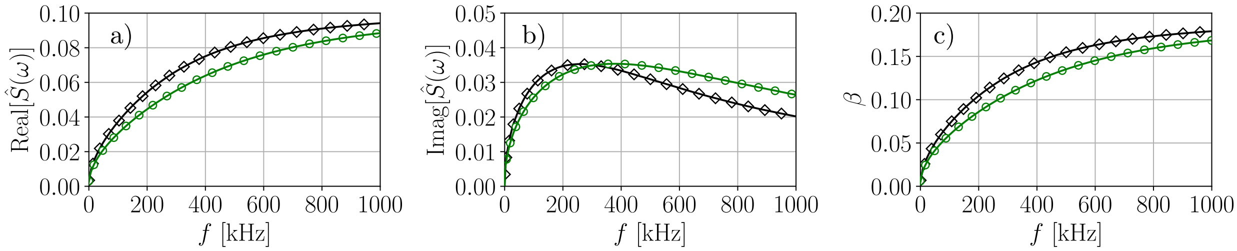

Figure 2: Real (a) and imaginary (b) components of the complex wall softness, $\hat{S}(\omega)$, representative of the C/C surface at wall pressure conditions and (c) corresponding acoustic absorption coefficient, β, at flow conditions related to $Re_m = 4.06 \cdot 10^6$ m^{-1} (○) and $Re_m = 6.43 \cdot 10^6$ m^{-1} (◇) as well as the multipole reconstruction of the complex signal following the vector fitting procedure (——).

shows a representative performance of this fitting procedure using the C/C material acoustic properties as an example. In this work, the estimation of C/C's surface averaged acoustic impedance are performed via fitting parameters of the homogeneous absorber theory (HAT) (Möser, 2009) to reflect experimentally measured results for the absorption coefficient

$$\beta(\omega) = 1 - |\hat{R}(\omega)|^2, \tag{23}$$

related to the acoustic power loss caused by thermoviscous dissipation inside the pores. The experiment compared the amplitude of ultrasonic waves reflected from the porous material A_{porous}, against a reference polished steel impermeable sample, A_{ref}, i.e. it evaluated the ratio $|\hat{R}| \sim A_{\mathrm{porous}}/A_{\mathrm{ref}}$ at various base pressures and discrete frequencies (Wagner et al., 2014). Ultimately, the calibration of the HAT model returns a good fit for the parameter values for flow resistivity, $\Xi = 13.6$ MPa s m^{-2} and structure factor, $\kappa = 7.9$, together with the known value of porosity of $\phi = 0.15$.

The implementation of TDIBC in a Navier-Stokes solver uses the relation between the complex wall softness coefficient, $\hat{S}(\omega)$, with the incident, $\hat{A}^-$, and reflected, $\hat{A}^+$, waves from a given surface (see figure 1) in the frequency domain via

$$\hat{S} = \frac{\hat{A}^+ + \hat{A}^-}{\hat{A}^-}, \tag{24}$$

to update the normal velocity boundary condition at each time step, an inverse Fourier transform is performed. Respecting causality, the convolution integral is then taken in the interval $[0, t]$, as demonstrated by Fung and Ju (2004), via

$$A^+(t) = -A^-(t) + \int_0^\infty S(\tau)A^-(t-\tau)d\tau, \tag{25}$$

where the time-domain definition of the incident and reflected waves are defined with respect to v' and p' are the fluctuating values of wall normal velocity and pressure respectively, as in (26).

$$\begin{cases} A^-(t) = v'(t) + p'(t)/\rho_0 a_0 \\ A^+(t) = v'(t) - p'(t)/\rho_0 a_0 \end{cases} \tag{26}$$

To numerically carry out the convolution integral shown in (25) and couple it with a Navier-Stokes solver, it needs to be evaluated at $t + \Delta t$, where Δt is a finite time interval used to advance the numerical solution in time, as

$$A^+(t+\Delta t) = -A^-(t+\Delta t) + \sum_{k=1}^{n_o} \left[s_k(t+\Delta t) + s_k^*(t+\Delta t) \right] \tag{27}$$

where the contribution of the k-th pole and residue pair (s_k) to the convolution integral can be expressed as

$$s_k(t+\Delta t) = \int_0^{\infty} \mu_k e^{p_k t} A^-(t+\Delta t-\tau)d\tau. \tag{28}$$

Using the internal addition property of the integral in 28, Scalo et al. (2015) showed that

$$s_k(t+\Delta t) = z_k s_k(t) + \int_0^{\Delta t} \mu_k e^{p_k t} A^-(t+\Delta t-\tau)d\tau, \tag{29}$$

where $z_k = e^{p_k t}$. Following Fung and Ju (2004), the integral in 31 is evaluated using a trapezoidal quadrature rule, which is second-order accurate in time. The resulting relation for the contribution of each pole and residue pair can be written as

$$s_k(t+\Delta t) = z_k s_k(t) + \mu_k \Delta t \left[w_{k0} A^-(t+\Delta t) + w_{k1} A^-(t) \right] \tag{30}$$

where

$$w_{k0} = \frac{z_k - 1}{p_k^2 \Delta t^2} - \frac{1}{p_k \Delta t} \quad \text{and} \quad w_{k1} = -\frac{z_k - 1}{p_k^2 \Delta t^2} + \frac{z_k}{p_k \Delta t}. \tag{31}$$

After the numerical evaluation of the convolution integral and after summing the contribution of each pole and residue pair, the outgoing wave (A^+) at time $t + \Delta t$ can be determined and, ultimately, the wall normal velocity can then be recovered and imposed at each time step as

$$v'(t+\Delta t) = \frac{1}{2}\left[A^-(t+\Delta t) + A^+(t+\Delta t) \right]. \tag{32}$$

As a final remark, a higher-order TDIBC implementation based on auxiliary differential equations was developed by Chen and Scalo (2021) and applied to the investigation of wall porosity effects on supersonic and hypersonic turbulent channels. In practice, no observable difference was found between the lower and higher-order formulations for the current application of hypersonic boundary layer simulations possibly due to small time step constraints. Ultimately, the second-order accurate approach was preferred due to its simplicity.

3 Axisymmetric Base Flow Stability Analysis

This section analyzes the evolution of small disturbances in an axisymmetric hypersonic flow setup over impermeable and porous walls modeled via the TDIBC. A 2.5 mm nose-tip radius was considered as per Wagner et al. (2013)'s experimental setup. The initial conditions of the laminar base state provided by a low-order precursor simulation performed using the DLR FLOWer code (Kroll and Fassbender, 2006). A more detailed description of these calculations can be found in Wartemann et al. (2014).

It is important to note that the simulations presented in the current section test the ability of the Quasi-Spectral Viscosity (QSV) approach (Sousa and Scalo, 2022) to correctly capture pure second-mode wave linear stability dynamics. The QSV closure is not required for the current axisymmetric runs, but it is necessary to stabilize the three-dimensional transitional simulations at the flow conditions ($T_w/T_{aw} \approx 0.1$) and grid resolutions considered, especially in the turbulent region.

A transient adjustment of the numerical solution on the computational grid is first observed after the initialization of the simulations for all Re_m and nose tip radii considered. All simulations are carried out until a steady state is reached, resulting in the profiles shown in figure 3, plotted for various streamwise locations. For all cases considered, an excellent agreement between the precursor results and simulated conditions is observed. As the Reynolds numbers increases, the boundary layer thicknesses decreases. Additionally, the blunt tip induces an entropy layer that affects the near-wall profiles leading to a thicker boundary layer near the leading edge. However, as the flow develops downstream, the relative importance of the nose tip bluntness in the flow decreases and the profiles eventually converge to those predicted by the self-similar conical Blasius. This determines the existence of two regions: one near the tip, where the high temperature

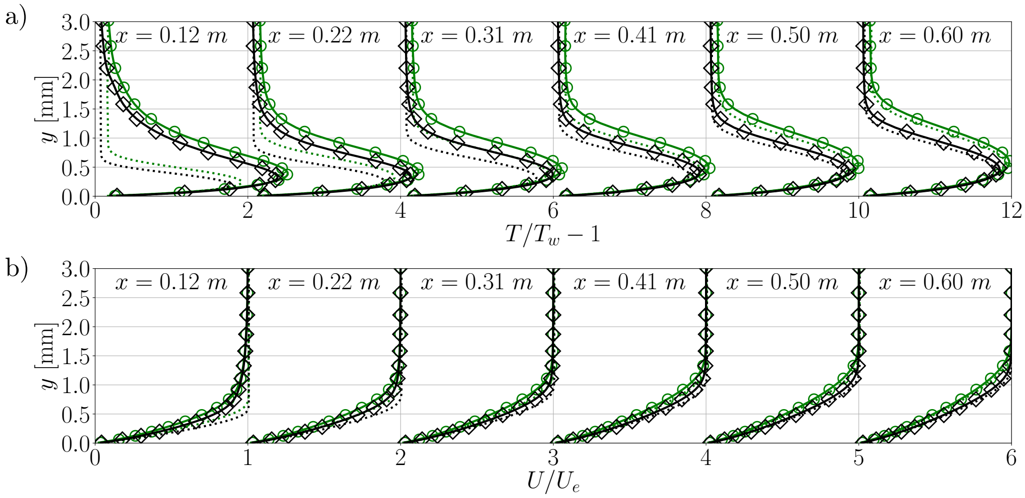

Figure 3: Temperature (a) and streamwise velocity (b) profiles for a 2.5 mm-tip cone at $Re_m = 4.06 \cdot 10^6$ m^{-1} (green) and $Re_m = 6.40 \cdot 10^6$ m^{-1} (black). Results from the unperturbed simulation (——) are compared against the similarity profile obtained from Mangler-transformed Blasius solution for a sharp cone (········) and the solution from the DLR FLOWer precursor simulation (○;◇). Color coding is consistent with table 1.

induced by the blunt shock thickens the boundary layer, followed by a zone where the boundary layer develops spatially slower than for the sharp cone case.

Following the establishment of an unperturbed laminar state for all cases, a broadband pulse disturbance is introduced via a low amplitude suction and blowing at the wall. The pulse is imposed with a period of $1/f_p$ where $f_p = 600$ kHz, therefore its broadband frequency space distribution is centered around f_p and is capable of exciting all the frequency range relevant for second-mode instabilities. The pulse is applied within a short streamwise strip equivalent to $x = (0.05 \pm 0.005)L_x$ as following:

$$v(x, y = 0, t) = \cos(\pi\xi)^3 \sin(2\pi f_p t), \quad \text{for } 0 \leqslant t \leqslant 1/f_p \tag{33}$$

where ξ is a normalized variable with values in the $[-1, 1]$ range, which is mapped to the actual extent of the strip where the pulse is applied. This perturbation aims at mimicking a natural transition scenario due to its broadband characteristics. It was first used by Gaster and Grant (1975) in incompressible transition simulations and by Sivasubramanian and Fasel (2014) to study its high speed counterpart. The same strategy was used by Sousa et al. (2019) demonstrating second-mode attenuation by an impedance boundary condition modeling the same C/C material considered in the present work but only on a sharp cone.

In this section such previous work is extended to include the effect on nose tip bluntness with a companion linear stability analysis assuming parallel flow. Porous walls are modeled with an impedance boundary condition introduced in the Navier-Stokes solver as a TDIBC (section 2.3) and, in the LST solver, directly in the frequency domain (see equation 19).

To ensure that the evolution of the high-frequency perturbations is accurately captured, a grid sensitivity study is performed over impermeable walls for the both Reynolds numbers considered and for each nose tip configuration. Results for the amplitude of the wall pressure perturbations are shown for a progression of grid resolutions in figure 4. Ultimately, the cases qualitatively converge.

The effects of surface boundary conditions on the evolution of a given Fourier component of the pulse disturbance are analyzed in figure 5 via the instantaneous wall pressure distribution for different frequencies, Reynolds numbers and nose tip bluntness. Considering that the porous insert is not present until $x \simeq 0.19$ m ($X = 0.182$ m), for any given Re_m and tip geometry, figure 5 shows that the amplitude of the surface pressure oscillations remain equivalent for both impermeable and porous simulations within this region. As the pulse evolves over the impedance boundary, a negative acoustic energy flux is established and energy is removed from the disturbance. The overall second-mode attenuation is achieved not only by decreasing the

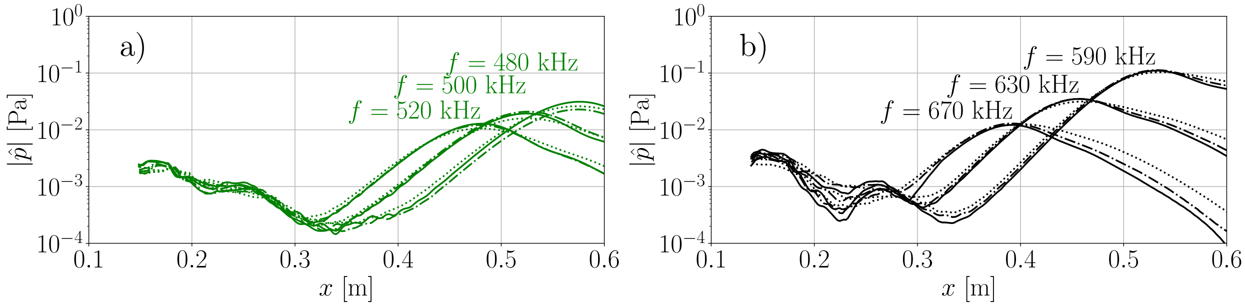

Figure 4: Grid sensitivity analysis for various frequency components of the wall pressure perturbation amplitude in an axisymmetric simulation of broadband pulse propagation over blunt cone. Results are shown for grid sizes: $n_x \times n_y = 2048 \times 96$ (⋯⋯); $n_x \times n_y = 3072 \times 144$ (-·-·-); and $n_x \times n_y = 4608 \times 192$ (——). Flow conditions are for Reynolds numbers: (a) $Re_m = 4.06 \cdot 10^6$ m^{-1} in green; and (b) $Re_m = 6.40 \cdot 10^6$ m^{-1} in black. See table 1 for the complete color scheme.

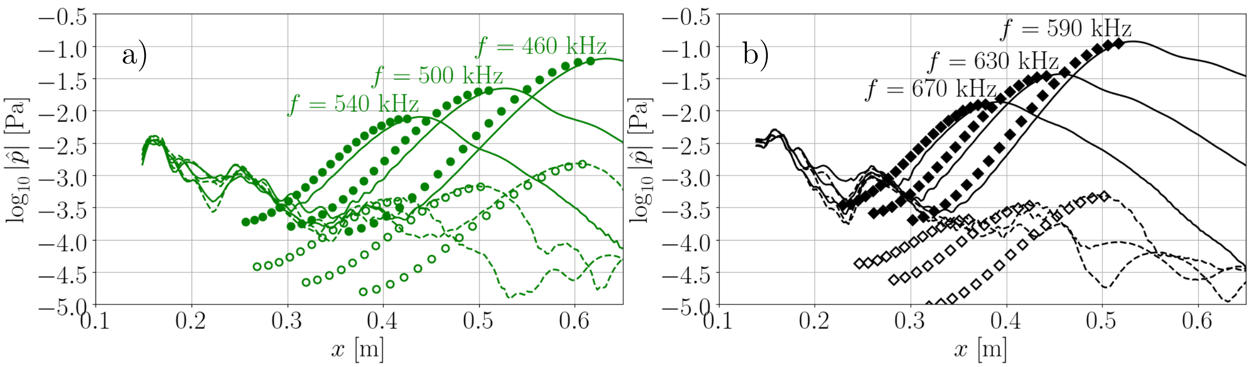

Figure 5: Comparison between QSV-LES simulations (lines), and LST (symbols) predictions for various Fourier components of wall pressure fluctuations as a function of space. Results are shown for a blunt nose tip geometry. Impermeable walls: —— and (◀, ●, ◆); porous walls: - - - - and (◁, ○, ◇). Flow conditions are for Reynolds numbers: (a) $Re_m = 4.06 \cdot 10^6$ m^{-1} in green; (b) $Re_m = 6.40 \cdot 10^6$ m^{-1} in black. See table 1 for the complete color and symbol scheme.

growth rates in the regions of instability but also by increasing the attenuation rates in the region where it is stable. The combination of both effects leads to the amplitude of the surface pressure oscillation signal over a porous surface to be always lower than over the impermeable surface.

Furthermore, these results are compared against a linear stability theory (LST) solver. Since the LST solver returns spatial growth rate information and not the absolute amplitude, a choice is made in the current work to show the amplitude of the signal reconstructed via backward integration starting from the second neutral point. This choice avoids the numerical evaluation of the spatial derivative of the wall pressure disturbance amplitude near the first neutral point, which is made noisy by the low amplitude values and can even rely below the numerical noise existent in the simulations, as is the case for the flow over the blunt-nosed geometries considered (figure 5).

Results from the high-order calculations for all cases considered follow closely the LST predictions, despite small discrepancies present specially over impermeable walls. The main reason for their occurrence is a mismatch between the LST-predicted location for the second neutral point. The magnitude of the predicted and recovered growth rates, though, are in agreement since a slight shift of the curves is sufficient to collapse the curves. The small discrepancies that are observed are attributed to nonlinear effects. This argument is corroborated by the fact that the agreement between LST and pulse advection simulations is improved when porous walls are considered for all cases. The attenuating effect of porous walls lead to smaller disturbances levels and decreased influence of nonlinear effects. Although some nonlinear effects are present, it is argued that it was necessary to perturb the simulations with the chosen amplitude level to allow the comparison between porous and impermeable walls, as well as between different nose tips and flow conditions. It can be seen in figure 5 that the recovered signal over porous walls when a blunt-nosed geometry is considered is barely above the floor noise level.

Comparing the results obtained from the numerical simulations of the advection of a broadband disturbance with the ones predicted by linear stability theory, one can reach two conclusions: first, that the implementation of the TDIBC technique in the Navier-Stokes solver is numerically consistent between different solvers, and second, that the use of the QSV technique does not hinder the capability of accurately simulating the second-mode's instability dynamics. In the remainder of the manuscript the same numerical framework will be used to simulate the complete transition path to turbulence and how the structure of the latter is affected by the presence of a porous surface.

4 Transitional Boundary Layer Simulations

In this section, the same flow conditions and cone geometries used for the axisymmetric simulations reported in section 3 are analyzed with the addition of an 8-degree azimuthal extension to the computational domain to capture the transition process over impermeable and porous walls.

4.1 Three-Dimensional Forcing

The base laminar flow is perturbed in a localized region of space by imposing grid independent pressure (p') and corresponding isentropic density fluctuations,

$$\rho' = p'/a_0^2, \tag{34}$$

where a_0 is the local speed of sound of the base state. These are used to impose the total fluctuating pressure and density fields, which drive the momentum (5) and energy conservation (6) equations, yielding corresponding velocity and temperature fluctuations. The natural hypersonic boundary dynamics outside of the forcing region then induce growth on particular modes of the perturbation field, ultimately leading to transition.

The functional form of the introduced pressure disturbance field is written as,

$$p'(\mathbf{x},t) = p_{rms}\frac{\phi'}{\sigma(\phi')}, \quad \text{where} \quad \phi' = \sum_{m=0}^{28} \phi'_m(\mathbf{x},t,f_m), \tag{35}$$

and where ϕ' is constructed by overlapping uniformly distributed pseudorandom scalar fields (ϕ'_m) between -1 and 1 for each frequency component (f_m) generating the final perturbation spectrum. A Fourier transform is then applied in three-dimensions for each m^{th} scalar field and the higher wavenumber coefficients, corresponding to spatial modes not resolvable on the coarsest grid considered, are discarded.

An inverse FFT is then taken and the resulting three-dimensional field of complex coefficients (K_m) is used to reconstruct the m^{th} frequency component of the pressure fluctuation field as,

$$\phi'_m(\mathbf{x},t,f_m) = A(f_m)\text{Real}\left(K_m(\mathbf{x})e^{-j2\pi f_m t}\right), \tag{36}$$

where $A(f)$ is the amplitude of the disturbance signal as a function of frequency, reconstructed based on measurements made in the HEG wind tunnel (Wagner et al., 2018) and given by

$$A(f) = 0.00448e^{-0.02009f} + 0.00131. \tag{37}$$

The pressure disturbance levels in the HEG tunnel decay monotonically with frequency. Ultimately, we introduce the disturbance field as a linear combination of the individual disturbance fields for each frequency in the range of 50 kHz to 890 kHz at each 30 kHz, i.e.

$$f_m = 50 + 30m \text{ kHz}. \tag{38}$$

The total perturbation field achieved through this method is normalized by its standard deviation (σ) estimated using a period equivalent to the five times the largest time scale of the imposed perturbation field, in this case equivalent to 20 μs, and the root mean squared pressure amplitude (p_{rms}) is chosen as free parameter.

In the current simulations, $p_{rms}/p_\infty = 3\%$ was chosen after some iterations and fair agreement with the experimental results is achieved (see figure 7). This is in the same order of the perturbation amplitude of $p_{rms}/p_w = 2.5\%$ observed in Wagner et al. (2018) The laminar base state was perturbed near the inflow and close to the wall in a volume of dimensions equal to $\ell_x = 0.075L_x$, $\ell_y = 0.002$ m and $\ell_\theta = 8.0$ degrees, where L_x is the simulation's extent in the streamwise direction (see table 2), as shown in figure 6.

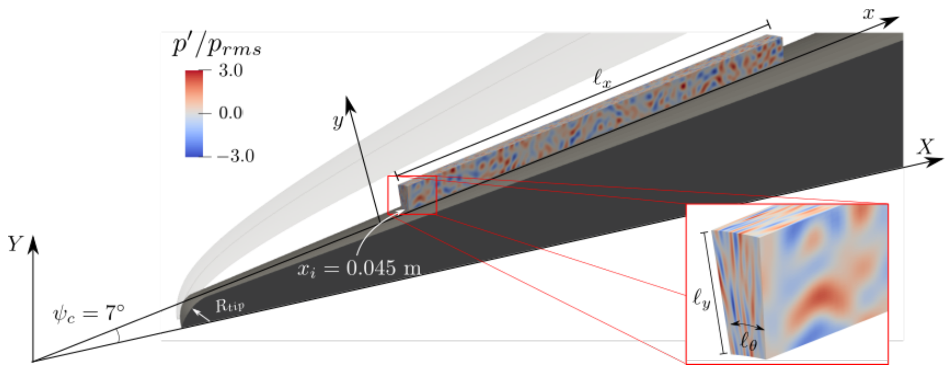

Figure 6: Visualization of forcing volume with dimensions, $\ell_x = 0.075L_x$, $\ell_y = 0.002$ m and $\ell_\theta = 8.0$ degrees, with L_x being the computational domain extent in the streamwise direction (see table 2). Hyperbolic tangent functions are used to smoothly transition to the unperturbed regions over a quarter of the forcing volume's extent in both the streamwise and wall normal directions.

4.2 Comparison against experiments: Wall Heat Flux

Previous literature has used a lot of Stanton number (St) and normalized streamwise distance (Re_x) to identify the transition between laminar to turbulent conditions. This choice is able to collapse different flow conditions into a single curve that identifies the laminar and turbulent heat transfer correlation values but, when used in transitional simulations it can falsely convey the idea that the transition location is anticipated for higher free stream Reynolds number (Re_m). For this reason heat flux results in figure 7 are displayed versus the axial cone coordinate X and normalized by the corresponding laminar value at $X = 0.275$ m. The use of such a coordinate system allows to display the anticipation of the turbulence onset that occurs as the Re_m increases but it also leads to a variation of the value of the fully turbulent heat-flux correlation curves with Re_m.

Various grid refinement levels are reported in figure 7, where it can be observed that the results for the normalized averaged heat flux distribution along the streamwise direction are converging as the resolution increases. The initial resolution increase step from a coarse ($2048\times96\times48$) to an intermediate ($2560\times120\times64$) level leads to a higher adjustment on the transitional front location and the maximum magnitude of the turbulent heat flux than the following step from intermediate to fine ($3072 \times 144 \times 80$) resolution. That is observed when either an impermeable or porous boundary condition is considered. This behavior further supports the soundness of the dynamic LES approach adopted in the current work.

Figure 7 also shows that the current LES performed over a blunt-nosed cone at $Re_m = 6.40 \cdot 10^6$ m^{-1} is not able to reach the fully turbulent heat flux predicted Van Driest's correlation (White and Corfield, 2006), differently than what is observed for the lower Re_m experimental conditions. Two reasons are behind this result. First, the transition over a blunt geometry happens further downstream in the computational domain than in the sharp cone simulations. Due to the present grid arrangement (see figure 1), both wall-normal and azimuthal resolutions decrease in the streamwise direction. Second, the higher Re_m increases the grid resolution requirements for the LES to capture the value of the fully turbulent heat flux. In spite of this,

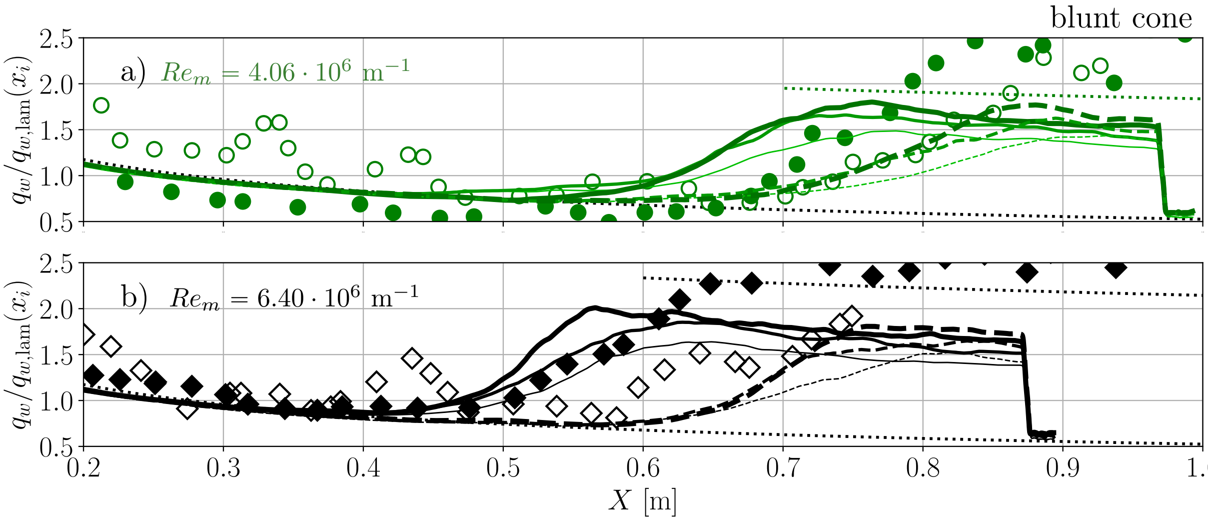

Figure 7: Average heat flux from experimental measurements (symbols) and simulation results (lines) for 2.5mm-blunt-nosed cone, plotted versus the streamwise distance from the tip of the cone. Results from coarser to finer grid refinement levels ($2048 \times 96 \times 48$, $2560 \times 120 \times 64$ and $3072 \times 144 \times 80$) are shown with progressively increasing line width. The heat flux is plotted normalized by the laminar value corresponding to the first measurement location at $X_i = 0.275$ m. Laminar and turbulent correlations are then being normalized accordingly (········). Over impermeable walls: —— and ◀, ●, ◆; over porous walls: - - - - and ◁, ○, ◇. Results are shown for Reynolds numbers: (a) $Re_m = 4.06 \cdot 10^6$ m^{-1} in green; and (b) $Re_m = 6.40 \cdot 10^6$ m^{-1} in black. See table 1 for the complete color scheme.

the LES predicts well the slope of the transitional heat flux curve, i.e. the intermittency structure, observed in the experimental values, and reaches grid convergence of the transition location.

Furthermore, although the data in figure 7 indicates that the impermeable wall simulations undergo transition to turbulence before the experiments for all of the cases considered, good agreement with the experimental values is recovered in the sharpness and spatial extent of the transitional regions. Ultimately, the precise transitional location is directly affected by the chosen amplitude of the fluctuations introduced in the near-tip region through the three-dimensional forcing procedure and better matching could be achieved if further (rather costly) iterations were made to calibrate the required p_{rms} level more precisely.

Figure 7 shows that the time-domain impedance boundary condition (TDIBC) is able to introduce the effect of the porous C/C in the flow field by delaying the turbulence transition front in comparison to the impermeable wall simulations. However, when the numerically-obtained transition delay results are compared against the corresponding experimental values, a slight over-attenuation of the transition dynamics is observed. Since linear stability results (figure 5) confirm that the TDIBC procedure is able to accurately impose the complex wall-impedance value, there is a possibility that the introduction of perturbations only in the near-tip region does not accurately reflect the reality of the experiments, where noise is received by the boundary layer at all spatial locations from the freestream. This difference may exaggerate the transition delay due to porous walls compared with the experiments. The analysis of the effects of various forcing strategies on the resulting extent of the transition delay offset is left for future work.

Additionally, uncertainties in the experimental measurements of the C/C surface impedance and roughness introduced by the porous material could also lead to differences in the transition location observed experimentally when compared to the one predicted numerically. In spite of this, the simulation results agree well with experiments when the slope and extent of the transitional region over porous walls are considered. Additionally, one can observe (figure 7) that an increase in Re_m leads to a greater transition delay capability for both simulated and experimentally-obtained results what was expected due to the increased acoustic absorption coefficient at the higher Re_m experimental conditions (see figure 2).

Although the mean heat flux spatial profiles show a gradual transition between laminar and turbulent correlation values, the transition process itself is not truly steady. Figure 8 shows that the standard deviation

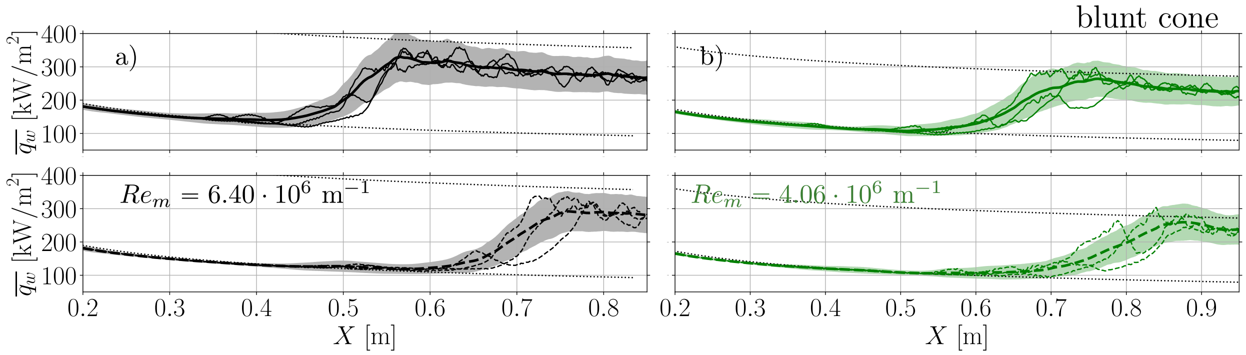

Figure 8: Wall heat flux results are shown for 2.5 mm blunt-nosed cones. Overall time-averaged results are shown in thicker lines with a shaded region with width equivalent to one standard deviation. Instantaneous spanwise-averaged values (thin lines) are filtered in the streamwise direction to remove the high wavenumber oscillations. Results are shown over impermeable (——) and porous (- - - -) walls and for Reynolds numbers: (a) $Re_m = 4.06 \cdot 10^6$ m^{-1} in green; and (b) $Re_m = 6.40 \cdot 10^6$ m^{-1} in black. See table 1 for the complete color scheme.

of the mean heat flux in the transitional region is higher than the laminar portion, being closer to the observed values in the fully turbulent region for all cases considered. This effect is most evident in the flow over blunt-nosed cones, where an approximately 5-fold increase in the standard deviation is observed.

Figure 8 also shows the filtered streamwise distribution of the instantaneous spanwise-averaged heat flux to showcase the possibility that, in some time instants, the local heat flux can be much higher than the overall time-averaged value. This is the result of the presence of fully turbulent spots in the transitional region for both impermeable and porous walls separated by weakly turbulent regions, seen in figure 9 for a 2.5 mm blunt-nosed cone at $Re_m = 4.06 \cdot 10^6$ m^{-1}. The existence of turbulent spots in the transitional region is the cause for an increased standard deviation and, ultimately, this could dictate more stringent requirements for thermal protection systems than what would be inferable from the average heat flux data along, due to the periodic overshoot to the fully turbulent heat flux values.

4.3 Comparison against experiments: Frequency Content

The question of whether the current computational approach can be used to replicate transitional flow measurements by Wagner et al. (2013) in the HEG wind tunnel is further addressed.

Figure 10 shows a comparison between the peak wall pressure disturbance frequencies measured experimentally in the HEG tunnel and the frequency of the maximum pressure oscillation amplitude of the equivalent signal gathered through numerical simulations. Additionally, the frequencies with the maximum growth rate predicted by LST are shown with a dot-dashed line (-·-·-) with a shaded region showing the frequency band of positive growth rate, between the higher and lower neutral frequencies. The spectrum of small-amplitude linear second-mode wave packet in a laminar boundary layer is expected to lie between the maximum growth rate line and the upper neutral frequency. In this region, the initially low-amplitude perturbations at a certain frequency would have experienced most of the expected integrated growth and should have the highest magnitude.

The experimental measurements for the $Re_m = 1.43 \cdot 10^6$ m^{-1} case, lie within the expected LST-predicted range. On the other hand, the experimental data gathered at higher Re_m consistently reports lower frequencies of maximum amplitude for a certain streamwise distance from the tip. Most of the measurements for the higher Re_m are made in regions where disturbance amplitudes are large enough to induce nonlinear interactions and mean flow distortions, causing measurable departure from laminar base flow dynamics predicted by linear theory. In fact, results from the present three-dimensional transitional simulations confirm the frequency shift to lower values observed in the experimentally measured values.

Numerical results reported in figure 10 show that the most amplified frequencies in the near tip lie are consistent with LST predictions, while progressively shifting to lower values as the flow approaches

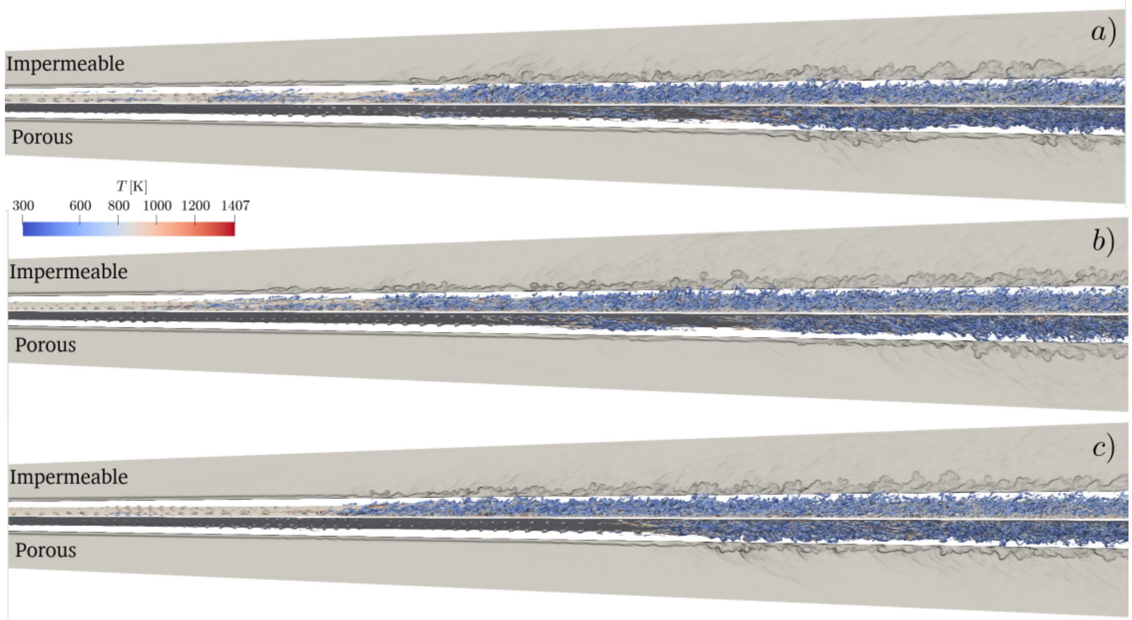

Figure 9: Instantaneous Q-criterion isosurfaces colored by temperature as well as a numerical Schlieren plane for times: (a) t_0; (b) $t_0 + 39.2$ μs; and (c) $t_0 + 78.4$ μs for a 2.5 mm blunt-nosed cone at $Re_m = 4.06 \cdot 10^6$ m^{-1} over impermeable and porous surfaces.

the transition location. In the turbulent region, higher frequencies and standard deviations are observed in comparison with the laminar portion of the flow due to the broadening of the spectra in that region (see figure 17). The surface distribution of the frequencies corresponding to the maximum pressure spectrum amplitude reveals patches of relatively lower frequencies surrounded by regions of higher values. This indicates the presence of streak-like distributions of the frequency content of the instantaneous surface pressure field.

Although a high variability of the frequency of the most amplified modes values is observed in the surface plots, both experimental and spanwise-averaged numerical results consistently agree on the shift to lower frequencies. Two reasons are behind this behavior. First, the width of the low-frequency streaks is smaller than the sensitive diameter of the PCB sensor used in Wagner et al. (2013), and both experimental and numerical results can be considered spanwise-averaged. Second, the low-frequency streaks carry the bulk of the perturbation energy. This phenomenon can be observed in figure 11 for a sharp and blunt-nosed cone geometries, respectively. These figures show the relation between the low heat-flux streaks and the lower frequency regions of the most amplified modes, which happen in spatially similar locations at the surface of the cone for all cases considered. Furthermore, an instantaneous visualization of the pressure oscillation field at the wall indicates the concentration of the high-amplitude oscillations at such locations. In conclusion, a spanwise average of the pressure fluctuation spectrum will always yield an overall downshift of observed frequency content with respect to linear stability predictions.

The cause of the shift to low frequencies is explained by the presence of streamwise vorticity in the flow field. It brings hot temperature fluid from the bulk of the boundary layer closer to the wall, as well as bringing cold fluid from the near-wall region further into the boundary layer. This is phenomenon is observed in the instantaneous temperature field contours shown in figure 12 and is responsible for the observed streak pattern. The region where low heat flux is predominant is connected to a locally thicker boundary layer and, consequently, a lower frequency perturbation spectrum.

In conclusion, the results gathered in figures 10 and 11 indicate that, for the freestream conditions studied, the initial second-mode instability promotes the formation of streamwise streaks which, in turn, lead to a downshift in the expected frequency spectrum.

An interesting result is observable for both cases considered, figure 11 shows that the low heat flux streaks formed in the transitional region of the flow persist well downstream of the streamwise locations where

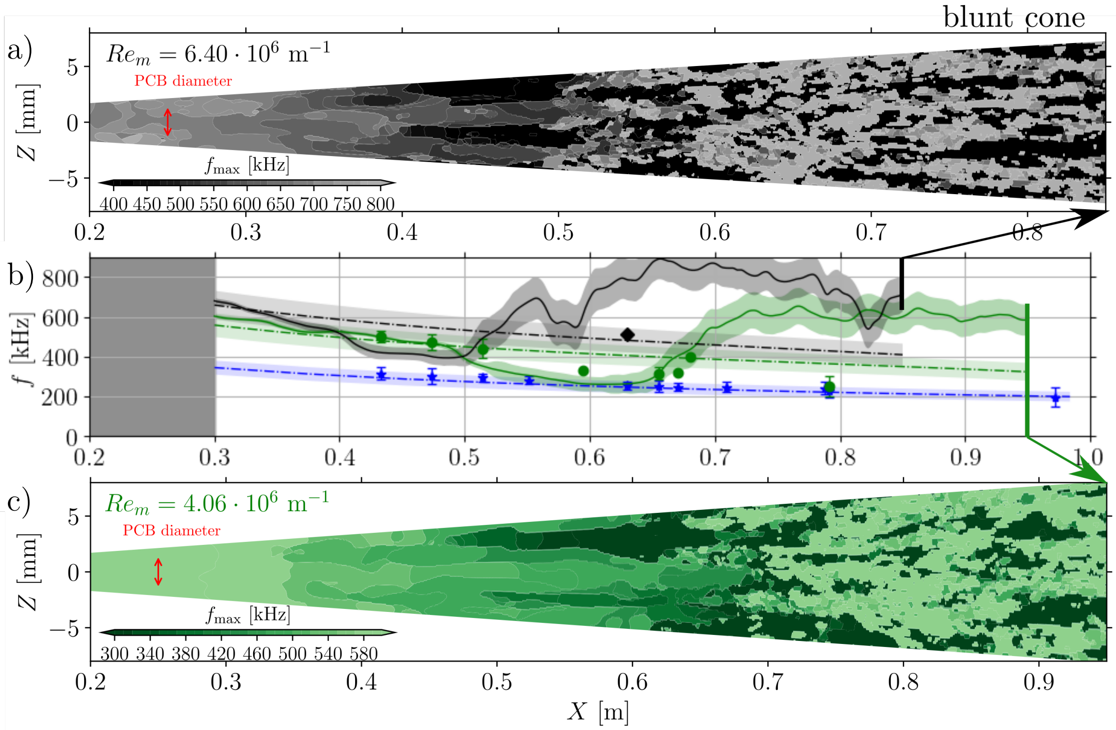

Figure 10: At the center (b), the frequencies connected to the maximum amplitude of the spanwise-averaged power spectrum density of the wall pressure oscillation signal over a 2.5 mm blunt-nosed cone are compared with the measured second-mode peak frequencies by Wagner et al. (2013) in experiments at the HEG wind tunnel. Simulated results are shown in solid lines and a shaded region equivalent to one standard deviation and experimental results are shown in symbols (★,●,◆) with their respective error bars. Additionally, the linear unstable region for each freestream condition is shown around the location of maximum growth, indicated by dash-dotted lines (-·-·-). The shaded region represents the approximate region where the entropy layer stabilizes the second-mode. Additionally, the spatial distribution of the frequencies of maximum amplitude is shown for $Re_m = 6.40 \cdot 10^6$ m^{-1} (a) and $Re_m = 4.06 \cdot 10^6$ m^{-1} (c). A red arrow is used to indicate the relative size of the sensitive surface diameter of the PCB pressure transducers used in Wagner et al. (2013)'s experiments to the streaks present in the flow. See table 1 for color scheme.

the peak in heat flux numerical measurements occurs. From that point on the flow regime is considered fully turbulent. The continued presence of the low heat flux streaks in the fully turbulent region indicate that memory from the earlier stages is retained and affect the turbulent flow. Moreover, the contours of instantaneous pressure oscillation at the surface indicate that there is a correlation between the location of the persistent low heat flux streaks and the second-mode-like pressure oscillations that occur in the turbulent region. Similar wave trains of wall pressure oscillations were observed in hypersonic turbulent channel flow simulations by Chen and Scalo (2021) at $M_b = 6.0$ over impermeable and porous walls. In that work, it was also reported that walls with relatively high permeability, much higher than what is measured for the porous C/C material considered in this work, can render such waves linearly unstable, further increasing their importance in the flow field dynamics.

4.4 Path to turbulence over impermeable and porous walls

The evolution of the averaged flow variables and fluctuation intensity profiles as the boundary layer transitions to a fully turbulent state over a blunt-nosed cone is analyzed. Figure 13 shows the normalized streamwise velocity and temperature profiles for both impermeable and porous surfaces as a function of the distance from the tip of the cone at $Re_m = 4.06 \cdot 10^6$ m^{-1} and $Re_m = 6.40 \cdot 10^6$ m^{-1}. Closer to the cone

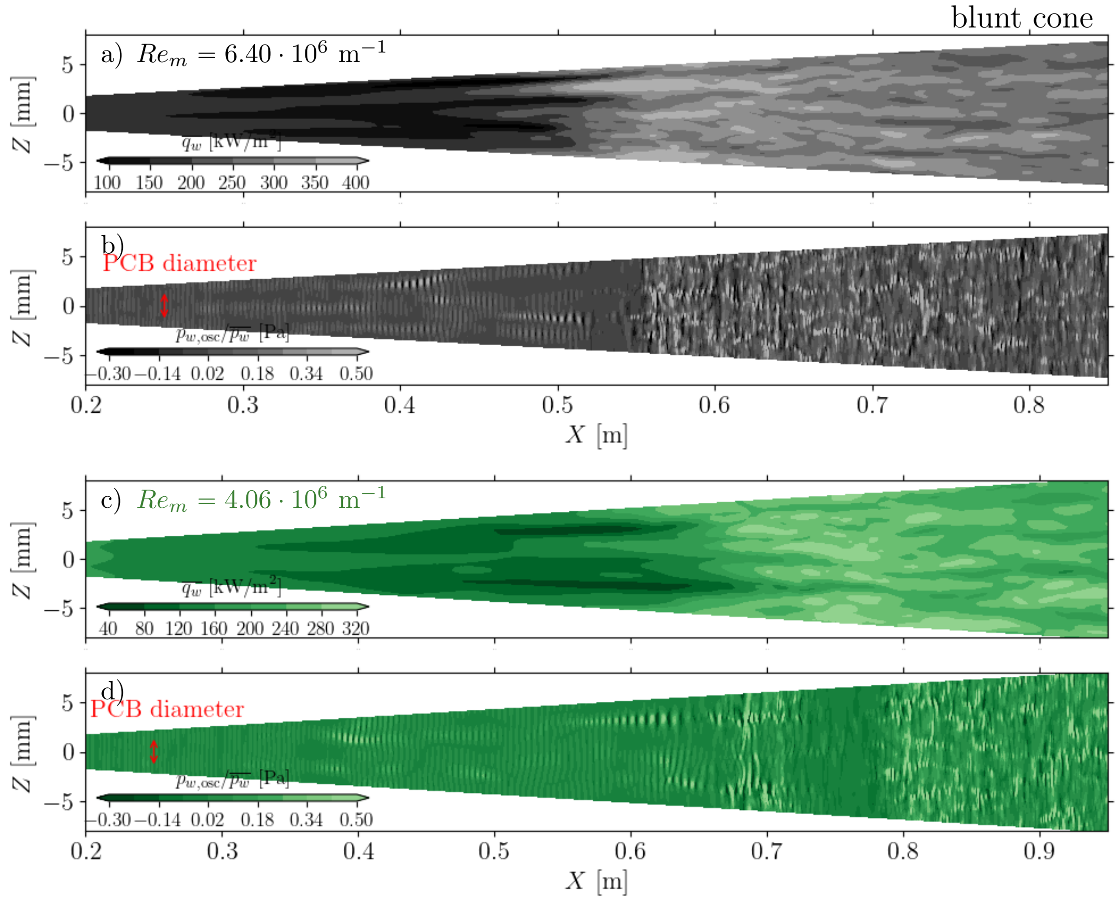

Figure 11: Surface distribution of averaged wall heat flux (a, c) as well as instantaneous visualization of normalized wall pressure oscillations (b, d) are shown for a 2.5 mm blunt-nosed cone at $Re_m = 6.40 \cdot 10^6$ m^{-1} (a, b) and $Re_m = 4.06 \cdot 10^6$ m^{-1} (c, d). A red arrow is used to indicate the diameter of the sensitive surface a the PCB pressure transducers used in Wagner et al. (2013), comparing it against the streaks present in the flow. See table 1 for the complete set of colors and symbols used.

nosetip, the profiles for both quantities are similar to the laminar ones predicted for laminar flow conditions. This indicates that the imposed perturbation field does not have enough energy to distort the mean flow. As the disturbances move downstream their amplitude grow and a gradual departure from the laminar profile is observed. The flow over an impermeable surface shows a faster evolution towards a thicker boundary layer and higher near-wall gradient when compared against the flow over porous walls for both Re_m considered, showing an effective transition delay.

Further insight into the effects of porous walls on the transition path to a fully turbulent state can be gathered by plotting the mean streamwise velocity normalized in wall units. In the study of compressible turbulence, the transformation developed by van Driest (1951),

$$U^+_{\mathrm{VD}} = \int_0^{\overline{U}/u_\tau} \left(\frac{\overline{\rho}}{\rho_w}\right)^{1/2} d(\overline{U}/u_\tau), \tag{39}$$

and plotted against the local wall coordinate,

$$y^+ = \frac{y\rho_w u_\tau}{\mu_w} \quad \text{where} \quad u_\tau = \sqrt{\tau_w/\rho_w}, \tag{40}$$

has proven successful collapse of the data onto the incompressible log-law for adiabatic wall flow conditions. Increased heat transfer rates, though, lead to a departure from the incompressible log-law,

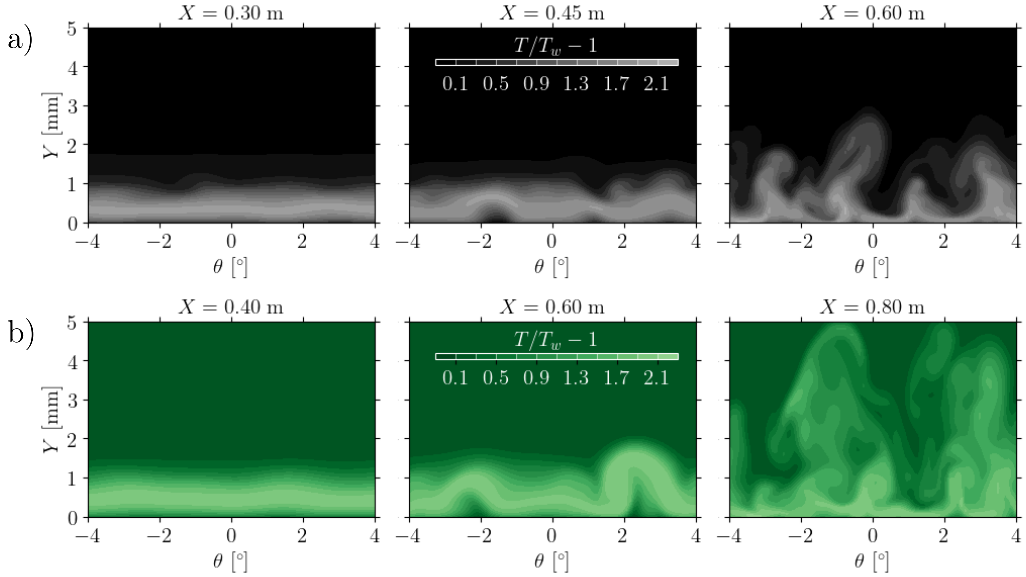

Figure 12: Instantaneous temperature profiles at different distances from the cone tip are shown for a 2.5 mm blunt-nosed cone at $Re_m = 6.40 \cdot 10^6$ m^{-1} (a) and $Re_m = 4.06 \cdot 10^6$ m^{-1} (b).

$$U^+ = \frac{1}{\kappa}\ln(y^{+/*}) + C \quad \text{where} \quad \kappa = 0.41, \tag{41}$$

exhibiting a larger intercept (C), decreasing the slope of the viscous sublayer (Trettel and Larsson, 2016; Zhang et al., 2018). This behavior is also observed in the current simulations where $T_w \approx 0.1\ T_{\text{aw}}$, as shown in figure 14. To achieve the desired collapse in the viscous sublayer, the mean velocity transformation proposed by Trettel and Larsson (2016),

$$U^+_{\text{TL}} = \int_0^{\overline{U}/u_\tau} \left(\frac{\overline{\rho}}{\rho_w}\right)^{1/2} \left[1 + \frac{1}{2}\frac{1}{\overline{\rho}}\frac{\partial \overline{\rho}}{\partial y}y - \frac{1}{\overline{\mu}}\frac{\partial \overline{\mu}}{\partial y}y\right] d(\overline{U}/u_\tau), \tag{42}$$

is used and plotted against the semi-local wall coordinate (Morkovin, 1962; Huang et al., 1995) given by

$$y^* = \frac{\overline{\rho}(y)u_\tau^*}{\overline{\mu}(y)}y \quad \text{and} \quad u_\tau^* = \sqrt{\overline{\tau_w}/\overline{\rho}(y)}. \tag{43}$$

Figure 14 shows that, by using this transformation, the correct viscous sublayer slope is recovered once fully turbulent conditions are achieved but, although the correct slope of the log-layer seems to be recovered, the TL transform is not able to collapse the data onto the incompressible log-law. Although the flow over impermeable walls reach fully turbulent conditions earlier in comparison to the flow over porous walls, no significant difference in the turbulent mean flow profiles is observed.

Zhang et al. (2018) performed a comprehensive analysis of DNS data in the Mach-number range $M = [2.5, 14]$ and $T_w/T_{\text{aw}} = [0.18, 1.0]$ and reported that, although Trettel and Larsson (2016)'s transformation is able to collapse the log-law intercept of hypersonic channel flows with incompressible data, it leads to an upwards shift when applied to high-speed flat plate boundary layers. An example of such behavior, also observed in the current dataset, is displayed in data from a DNS simulation with $M = 7.87$ and $T_w/T_{\text{aw}} \approx 0.5$ (Zhang et al., 2018), also plotted in figure 14.

Figure 15 shows profiles of velocity fluctuation intensity in the streamwise, wall-normal and azimuthal directions. Moving downstream, the flow characteristics become increasingly turbulent over both surface types considered and the characteristic peak of streamwise velocity fluctuations forms in the near wall region. This phenomenon happens spatially quicker for the flow over impermeable walls when compared to one over porous walls. Moreover, figure 15 also serves the purpose of determining the importance of

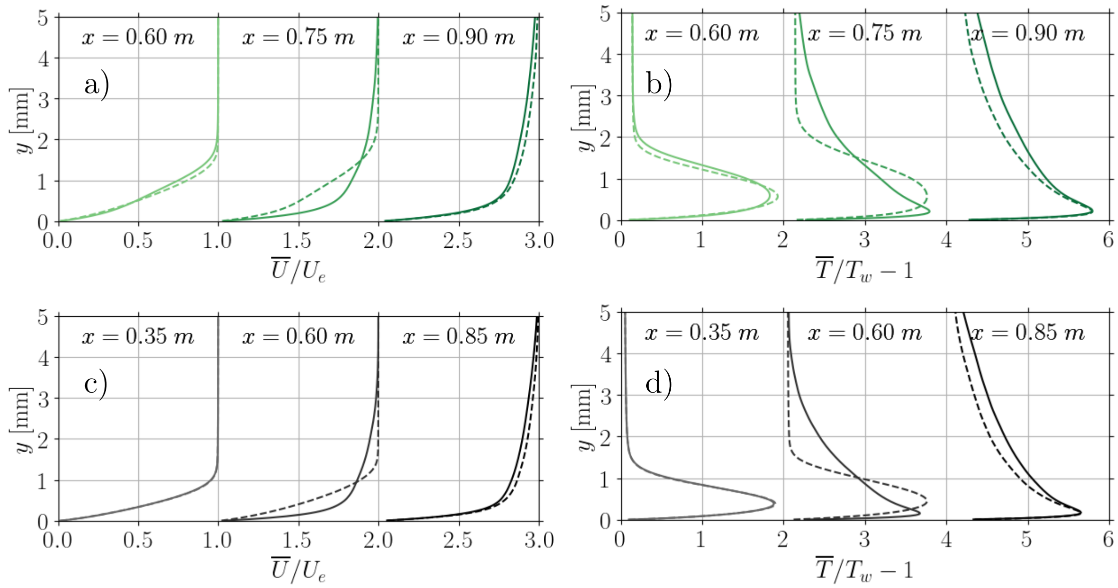

Figure 13: Reynolds-averaged streamwise velocity (a, c) and temperature (b, d) profiles for the following Reynolds numbers: (a, b) $Re_m = 4.06 \cdot 10^6$ m^{-1} (green); and (c, d) $Re_m = 6.40 \cdot 10^6$ m^{-1} (black) over a sharp cone with impermeable (——) and porous (- - - -) walls.

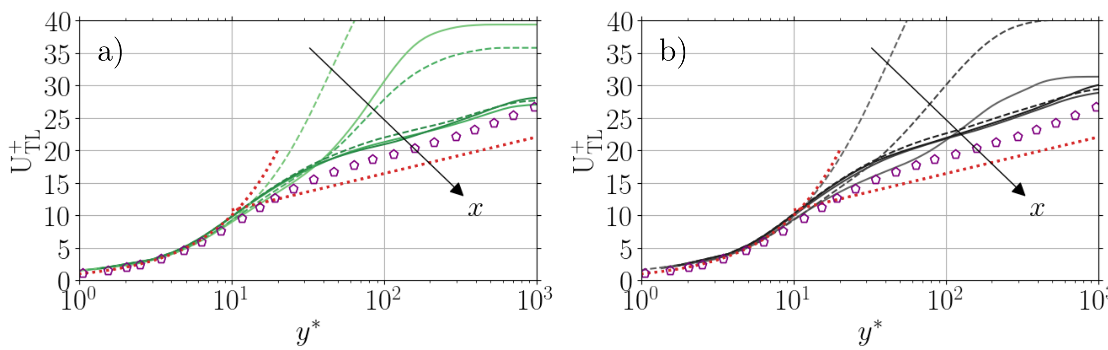

Figure 14: Mean streamwise velocity profiles m for Reynolds numbers: (a) $Re_m = 4.06 \cdot 10^6$ m^{-1} at $x = 0.65,\ 0.80,\ 0.95$ (green); and (b) $Re_m = 6.40 \cdot 10^6$ m^{-1} at $x = 0.55,\ 0.70,\ 0.85$ m (black) over a blunt-nosed cone, scaled based on Trettel and Larsson (2016)'s transformations. Results are shown over impermeable (——) and porous (- - - -) walls. The reference log-laws are displayed (········) for $\kappa = 0.41$ and $C = 5.2$. In symbols (⬠), DNS data by Zhang et al. (2018) for $M = 7.87$ and $T_w/T_{\mathrm{adb}} \approx 0.5$ over a flat plate.

the presence of surface porosity on the mean velocity fluctuation intensity profiles. Comparing the results obtained at the furthest downstream locations probed for both $Re_m = 4.06{\cdot}10^6$ m^{-1} and $Re_m = 6.40{\cdot}10^6$ m^{-1} freestream conditions, one can conclude that there is not a significant effect of porous walls representative of a C/C material on the flow field, apart from delaying transition to turbulence. It is noted that, however, the current modeling approach neglects distributed surface roughness effects, which may have an important hydrodynamic effect on the flow.

The contours of the intensity of the turbulent transport of thermal energy in the wall-normal direction are shown in figure 16. It is shown, due to the sign of the contour maps, that the turbulence-induced transport leads to the mixing of the highly concentrated hot fluid present in the inner portion of a laminar hypersonic boundary layer with colder fluid present both closer and further away from the wall. The mean transport of

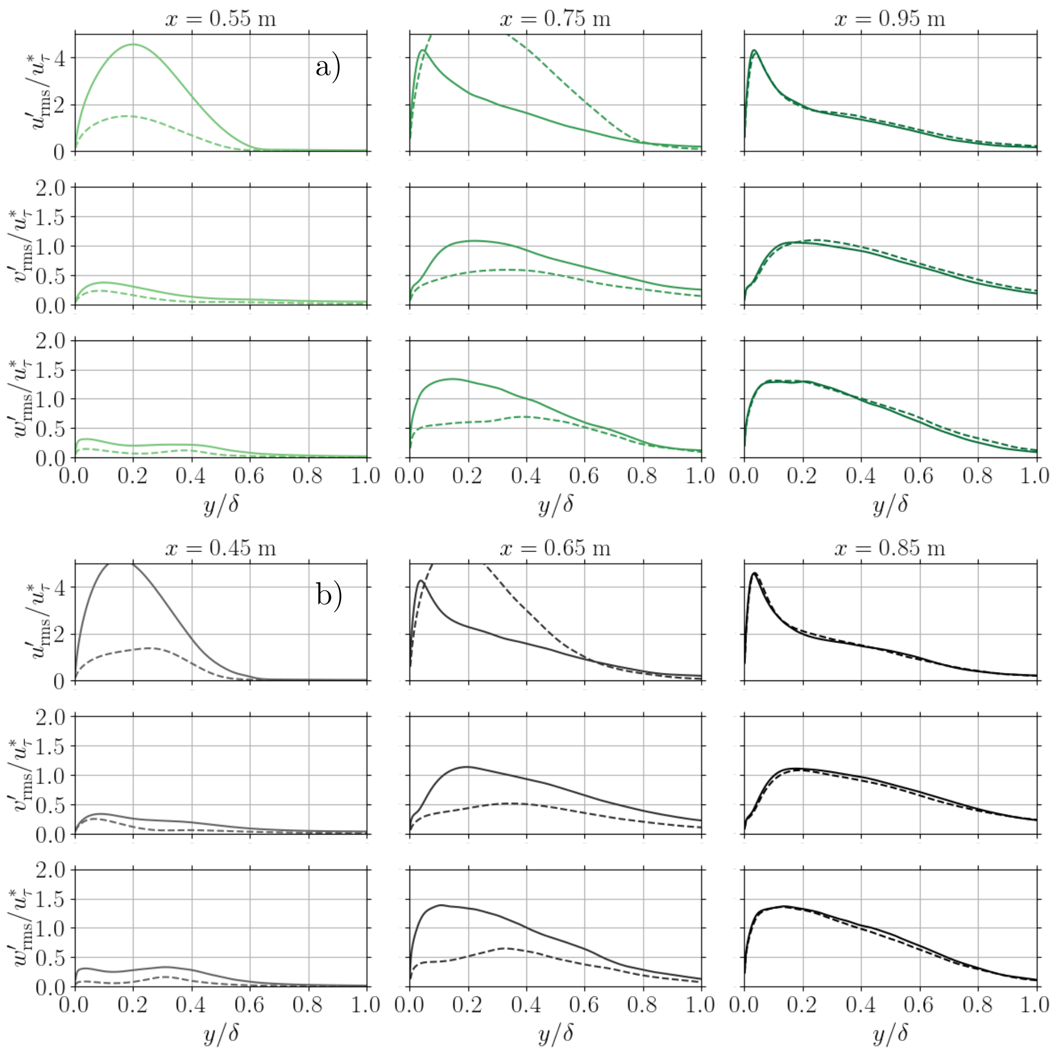

Figure 15: Velocity fluctuation intensity profiles for (a) $Re_m = 4.06 \cdot 10^6$ m^{-1} (green) and (b) $Re_m = 6.40 \cdot 10^6$ m^{-1} (gray) over a sharp cone with impermeable (——) and porous (- - - -) walls scaled by the local boundary layer thickness.

thermal energy towards the wall is responsible for the increase of the mean temperature in that region and, ultimately, for the increased the heat flux due to transition.

Near the cone nosetip for both Re_m, the wall pressure oscillation spectra over the two surfaces types shown in figure 17 display clear harmonics of a fundamental frequency being slightly attenuated over porous walls in comparison with impermeable walls. Moving further downstream, it is possible to observe that the flow over impermeable walls develops more rapidly into a fully turbulent state, characterized by a broader energy distribution, in comparison with the flow over a porous wall. Additionally, a peak frequency shift to lower frequencies for the flow over an impermeable surface when compared to the one over porous walls is also observed at $X = 0.50$ m for the $Re_m = 4.06 \cdot 10^6$ m^{-1} case and at $X = 0.45$ m for the $Re_m = 6.40 \cdot 10^6$ m^{-1} case. As previously discussed in subsection 4.3, this is an evidence of the presence of mean flow distortion that causes streamwise streaks and concentrates the pressure oscillations in the regions of increased boundary layer thickness over impermeable walls. Near the end of the computational domain the recovered spectra over impermeable and porous walls seem to converge, what is further evidence that the C/C's surface porosity delay's transition to turbulence but does not have a significant effect in turbulence itself.

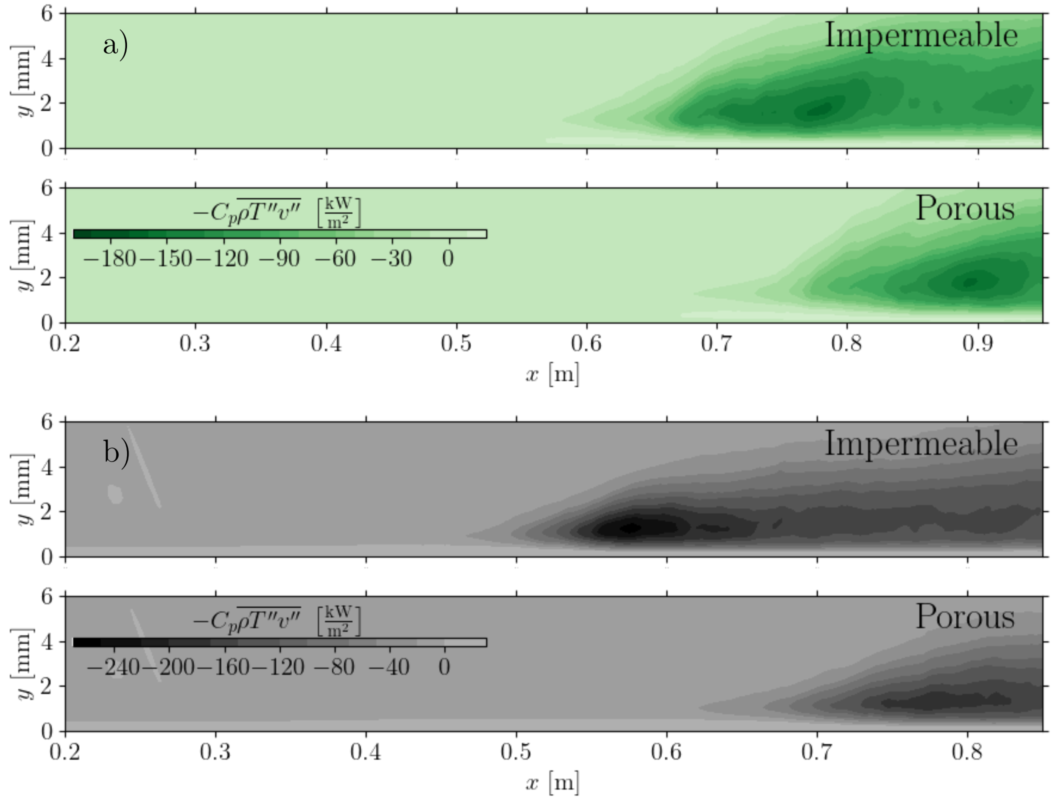

Figure 16: Contours of turbulent heat flux for for $Re_m = 4.06 \cdot 10^6$ m^{-1} (a) and $Re_m = 6.40 \cdot 10^6$ m^{-1} (b) over a 2.5 mm blunt-nosed cone with impermeable and porous walls.

5 Conclusion

Numerical simulations of hypersonic transition delay over a blunt-nosed cone due to the presence of porous walls were carried out. The simulations were designed to reproduce experiments performed by Wagner et al. (2013) on a 7°-half-angle cone at $M_\infty = 7.4$, which measured transition delay when porous carbon/carbon (C/C) surfaces were present. A broadband time domain impedance boundary condition (TDIBC) was used to introduce the porosity effects in the high-fidelity simulations. The use of this technique allows the application of the impedance boundary at all the frequencies concomitantly, which expands the modeling capacity used in previous numerical studies (Egorov et al., 2008; Wang and Zhong, 2011; Lukashevich et al., 2012), restricted to a frequency-by-frequency analysis. The current approach allows to assess the influence of a porous surface in a natural transition scenario, from the initial second-mode growth to the full breakdown to turbulence.

First, axisymmetric simulations are performed over impermeable and porous walls at different flow conditions, in which the second-mode is excited via the application of a broadband pulse. The spatial amplification of individual frequency modes compares favorably against linear stability analysis. The matching obtained supports the correct numerical implementation of the TDIBC and the dynamic behavior of the Quasi-Spectral Viscosity (QSV) closure Sousa and Scalo (2022). Following, three-dimensional simulations were performed and the boundary layer was excited with a grid-independent filtered pseudorandom pressure perturbations. These were received and amplified by the instability mechanisms inside the boundary layer leading to non-linear mode interactions and turbulent breakdown. During the transition process, an unstable frequency band shift to lower values was observed indicating a possible feedback from the mean flow distortion caused by nonlinear perturbations. The presence of the impedance boundary condition mimicking the C/C porous surface led to a slight over prediction of the transition delay that was observed in experiments. Although

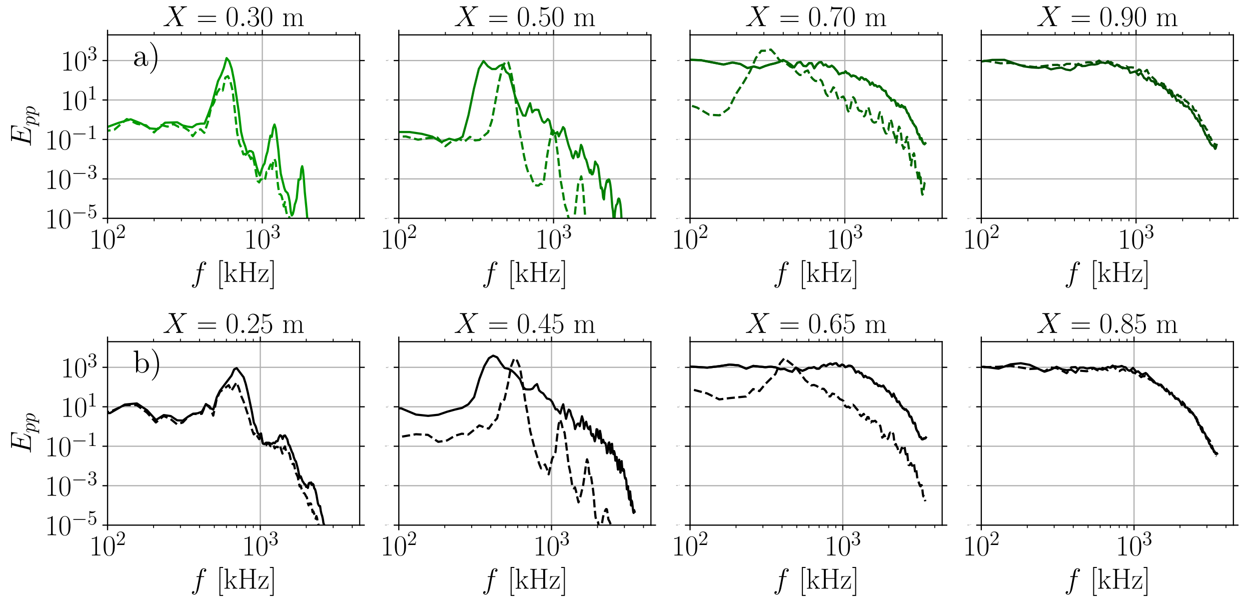

Figure 17: Energy spectra of wall pressure fluctuations for $Re_m = 4.06{\cdot}10^6$ m^{-1} (a) and $Re_m = 6.40{\cdot}10^6$ m^{-1} (b) over a 2.5 mm blunt-nosed cone with impermeable (——) and porous (- - - -) walls.

the presence of the porous surface was critical in delaying transition, it did not yield a significant change in the structure of the near-wall turbulence or the wall pressure oscillation spectra.

References

Y. Chen and C. Scalo. Trapped waves in supersonic and hypersonic turbulent channel flow over porous walls. *Journal of Fluid Mechanics*, 920, 2021.

Q. Douasbin, C. Scalo, L. Selle, and T. Poinsot. Delayed-time domain impedance boundary conditions (D-TDIBC). *J. Comput. Phys.*, 371:50–66, 2018.

L. Duan, I. Beekman, and M. Martin. Direct numerical simulation of hypersonic turbulent boundary layers. part 2. effect of wall temperature. *Journal of Fluid Mechanics*, 655:419–445, 2010.

L. Duan, I. Beekman, and M. P. Martin. Direct numerical simulation of hypersonic turbulent boundary layers. part 3. effect of mach number. *Journal of Fluid Mechanics*, 672:245–267, 2011. doi: 10.1017/S0022112010005902.

I. V. Egorov, A. V. Fedorov, and V. G. Soudakov. Receptivity of a Hypersonic Boundary Layer over a Flat Plate with a Porous Coating. *J. Fluid Mech.*, 601:165–187, 4 2008. ISSN 1469-7645. doi: 10.1017/S0022112008000669. URL `http://journals.cambridge.org/article_S0022112008000669`.

A. V. Fedorov, N. D. Malmuth, A. Rasheed, and H. G. Hornung. Stabilization of Hypersonic Boundary Layers by Porous Coatings. *AIAA Journal*, 39(4):605–610, 2001. doi: 10.2514/2.1382. URL `http://dx.doi.org/10.2514/2.1382`.

A. V. Fedorov, A. Shiplyuk, A. Maslov, E. Burov, and N. Malmuth. Stabilization of a Hypersonic Boundary Layer Using an Ultrasonically Absorptive Coating. *J. Fluid Mech.*, 479:99–124, 3 2003. ISSN 1469-7645. doi: 10.1017/S0022112002003440.

K. J. Franko and S. K. Lele. Breakdown mechanisms and heat transfer overshoot in hypersonic zero pressure gradient boundary layers. *Journal of Fluid Mechanics*, 730:491–532, 2013.

K.-Y. Fung and H. Ju. Time-Domain Impedance Boundary Conditions for Computational Acoustics and Aeroacoustics. *Int. J. Comput. Fluid D.*, 18(6):503–511, 2004.

M. Gaster and I. Grant. An Experimental Investigation of the Formation and Development of a Wave Packet in a Laminar Boundary Layer. In *Proceedings of the Royal Society of London A: Mathematical, Physical and Engineering Sciences*, volume 347, pages 253–269. The Royal Society, 1975.

B. Gustavsen and A. Semlyen. Rational approximation of frequency domain responses by vector fitting. *IEEE Transactions on power delivery*, 14(3):1052–1061, 1999.

K. Hannemann, J. Martinez Schramm, A. Wagner, and G. Ponchio Camillo. The high enthalpy shock tunnel göttingen of the german aerospace center (dlr). *Journal of large-scale research facilities JLSRF*, 4(A133): 1–14, 2018.

P. G. Huang, G. N. Coleman, and P. Bradshaw. Compressible turbulent channel flows: DNS results and modelling. *J. Fluid Mech.*, 305:185–218, 1995.

S. A. Jordan. A large-eddy simulation methodology in generalized curvilinear coordinates. *Journal of Computational Physics*, 148(2):322–340, 1999.

L. E. Kinsler, A. R. Frey, A. B. Coppens, and J. V. Sanders. Fundamentals of acoustics. *Fundamentals of Acoustics, 4th Edition, by Lawrence E. Kinsler, Austin R. Frey, Alan B. Coppens, James V. Sanders, pp. 560. ISBN 0-471-84789-5. Wiley-VCH, December 1999.*, page 560, 1999.

N. Kroll and J. K. Fassbender. *MEGAFLOW-Numerical Flow Simulation for Aircraft Design: Results of the second phase of the German CFD initiative MEGAFLOW, presented during its closing symposium at DLR, Braunschweig, Germany, December 10 and 11, 2002*, volume 89. Springer Science & Business Media, 2006.

S. K. Lele. Compact Finite Difference Schemes with Spectral-Like Resolution. *Journal of Computational Physics*, 103(1):16–42, 1992. ISSN 0021-9991. doi: 10.1016/0021-9991(92)90324-R.

J. Lin, C. Scalo, and L. Hesselink. High-Fidelity Simulation of a Standing-Wave Thermoacoustic–Piezoelectric Engine. *J. Fluid Mech.*, 808:19–60, Dec 2016. doi: 10.1017/jfm.2016.609.

S. Lukashevich, A. Maslov, A. Shiplyuk, A. Fedorov, and V. Soudakov. Stabilization of high-speed boundary layer using porous coatings of various thicknesses. *AIAA journal*, 50(9):1897–1904, 2012.

L. M. Mack. On the Inviscid Acoustic-Mode Instability of Supersonic Shear Flows. *Theoretical and Computational Fluid Dynamics*, 2(2):97–123, 1990.

N. Malmuth, A. Fedorov, V. Shalaev, J. Cole, M. Hites, D. Williams, and A. Khokhlov. Problems in High Speed Flow Prediction Relevant to Control. In *2nd AIAA, Theoretical Fluid Mechanics Meeting*, page 2695, 1998. doi: 10.2514/6.1998-2695. URL `http://dx.doi.org/10.2514/6.1998-2695`. (AIAA-1998-2695).

M. V. Morkovin. Effects of compressibility on turbulent flows. *Mécanique de la Turb.*, 367:380, 1962.

M. Möser. *Engineering Acoustics: an Introduction to Noise Control.* Springer Science & Business Media, 2009.

S. Nagarajan, S. K. Lele, and J. H. Ferziger. A Robust High-Order Compact Method for Large-Eddy Simulation. *Journal of Computational Physics*, 191(2):392–419, 2003.

S. Nagarajan, S. Lele, and J. Ferziger. Leading-Edge Effects in Bypass Transition. *J. Fluid Mech.*, 572: 471–504, 2007.

A. Rasheed, H. G. Hornung, A. V. Fedorov, and N. D. Malmuth. Experiments on Passive Hypervelocity Boundary-Layer Control Using an Ultrasonically Absorptive Surface. *AIAA Journal*, 40(3):481–489, 2002. doi: 10.2514/2.1671. URL `http://arc.aiaa.org/doi/abs/10.2514/2.1671`.

H. L. Reed, R. Kimmel, S. Schneider, D. Arnal, and W. Saric. Drag Prediction and Transition in Hypersonic Flow. In *AGARD Conference Proceedings*, volume 3, pages C15–C15. AGARD, 1997.

S. Rienstra. Impedance models in time domain, including the extended Helmholtz resonator modeli. In *12th AIAA/CEAS Aeroacoustics Conference (27th AIAA Aeroacoustics Conference)*, page 2686, 2006.

C. Scalo, J. Bodart, and S. K. Lele. Compressible Turbulent Channel Flow with Impedance Boundary Conditions. *Phys. Fluids*, 27(035107), 2015.

J. Sivasubramanian and H. F. Fasel. Numerical Investigation of the Development of Three-Dimensional Wavepackets in a Sharp Cone Boundary Layer at Mach 6. *J. Fluid Mech.*, 756:600–649, 10 2014. ISSN 1469-7645. doi: 10.1017/jfm.2014.434.

V. C. B. Sousa and C. Scalo. A unified Quasi-Spectral Viscosity (QSV) approach to shock capturing and large-eddy simulation. *Journal of Computational Physics*, 459:111139, 2022. ISSN 0021-9991. doi: https://doi.org/10.1016/j.jcp.2022.111139.

V. C. B. Sousa, D. Patel, J.-B. Chapelier, V. Wartemann, A. Wagner, and C. Scalo. Numerical Investigation of Second-Mode Attenuation over Carbon/Carbon Porous Surfaces. *Journal of Spacecraft and Rockets*, 56 (2):319–332, 2019. doi: 10.2514/1.A34294. URL `https://doi.org/10.2514/1.A34294`.

S. Thirani, P. Gupta, and C. Scalo. Knudsen number effects on the nonlinear acoustic spectral energy cascade. *Physical Review E*, 101(2):023101, 2020.

A. Trettel and J. Larsson. Mean velocity scaling for compressible wall turbulence with heat transfer. *Phys. Fluids*, 28:026102, 2016.

E. R. van Driest. Turbulent boundary layer in compressible fluids. *J. Aero. Sci.*, 18:145–160, 216, 1951.

B. Vreman, B. Geurts, and H. Kuerten. A priori tests of Large-Eddy Simulation of the compressible plane mixing layer. *Journal of engineering mathematics*, 29(4):299–327, 1995.

A. Wagner. *Passive Hypersonic Boundary Layer Transition Control Using Ultrasonically Absorptive Carbon-Carbon Ceramic with Random Microstructure.* PhD thesis, Katholieke Universiteit, Leuven, 2014.

A. Wagner, M. Kuhn, J. M. Schramm, and K. Hannemann. Experiments on Passive Hypersonic Boundary Layer Control Using Ultrasonically Absorptive Carbon–Carbon Material with Random Microstructure. *Experiments in fluids*, 54(10):1606, 2013.

A. Wagner, K. Hannemann, and M. Kuhn. Ultrasonic Absorption Characteristics of Porous Carbon–Carbon Ceramics with Random Microstructure for Passive Hypersonic Boundary Layer Transition Control. *Experiments in Fluids*, 55(6):1750, 2014.

A. Wagner, E. Schülein, R. Petervari, K. Hannemann, S. R. Ali, A. Cerminara, and N. D. Sandham. Combined free-stream disturbance measurements and receptivity studies in hypersonic wind tunnels by means of a slender wedge probe and direct numerical simulation. *Journal of Fluid Mechanics*, 842:495–531, 2018.

X. Wang and X. Zhong. The impact of porous surface on hypersonic boundary layer instability. In *40th Fluid Dynamics Conference and Exhibit*, 2010. AIAA-2010-5021.

X. Wang and X. Zhong. Phase Angle of Porous Coating Admittance and its Effect on Boundary-Layer Stabilization. In *41st AIAA Fluid Dynamics Conference and Exhibit*, page 3080, 2011.

V. Wartemann, A. Wagner, T. Giese, T. Eggers, and K. Hannemann. Boundary-layer stabilization by an ultrasonically absorptive material on a cone in hypersonic flow: numerical investigations. *CEAS Space Journal*, 6(1):13–22, 2014.

F. M. White and I. Corfield. *Viscous fluid flow*, volume 3. McGraw-Hill New York, 2006.

C. Zhang, L. Duan, and M. M. Choudhari. Direct numerical simulation database for supersonic and hypersonic turbulent boundary layers. *AIAA Journal*, 56(11):4297–4311, 2018.